buildings

MDPI

Article

Three-Dimensional Numerical Analysis on the Influence of Buttress Wall Removal Timing on the Lateral Deformation of Diaphragm Walls during Deep Excavation

Chia-Feng Hsu [1,*], Chung-Fu Kuan [2] and Shong-Loong Chen [3]

[1] Department of Civil Engineering, ChienKuo Technology University, Changhua City 500020, Taiwan
[2] ChienKuo Construction Co., Ltd., Taipei 106045, Taiwan; chungfu_kuan@ckgroup.com.tw
[3] Department of Civil Engineering, National Taipei University of Technology, Taipei 10608, Taiwan; f10391@ntut.edu.tw
* Correspondence: chiafeng1013@gmail.com; Tel.: +886-958-786-134

Abstract: Urban areas in Taiwan are densely populated with limited land. Excavation often takes place near existing buildings, necessitating protective measures for adjacent properties. Among these measures, cross walls or buttress walls are commonly employed, especially in weak foundation soils, which have seen many successful applications. These mechanisms mainly contribute to reducing lateral deformation of the diaphragm walls, ground subsidence, and excavation face uplift. However, the behavior of these walls is essentially three-dimensional, and common engineering analyses employing one-dimensional elastoplastic beam analysis cannot adequately simulate their mechanical behavior. This study utilized the PLAXIS 3D 2018 software to analyze real-life cases of buttress walls and cross walls. Then, the results of the numerical models were validated against actual field measurements, and the outcomes were satisfactory, and within the regulatory allowable values. The primary objective of this study was to find the influence of different buttress wall removal timings on the lateral deformation of the diaphragm wall. The findings suggest that the gradual removal of buttress walls will effectively control the lateral deformation of diaphragm walls during the excavation of deeper floors like mezzanines.

Keywords: diaphragm wall; deep excavation; weak foundation soils; buttress walls; removal timing

Citation: Hsu, C.-F.; Kuan, C.-F.; Chen, S.-L. Three-Dimensional Numerical Analysis on the Influence of Buttress Wall Removal Timing on the Lateral Deformation of Diaphragm Walls during Deep Excavation. *Buildings* **2023**, *13*, 2678. https://doi.org/10.3390/buildings13112678

Academic Editor: Suraparb Keawsawasvong

Received: 1 October 2023
Revised: 17 October 2023
Accepted: 19 October 2023
Published: 24 October 2023

1. Introduction

Land utilization remains a pertinent challenge in Taiwan's metropolitan regions. To maximize space, existing buildings are either renovated or replaced by new structures that expand vertically and increasingly, underground. Consequently, foundations are being dug deeper, expanding the scope of deep excavation projects. The Taipei Basin predominantly comprises thick layers of soft clay, known for its high water content and weak consistency. To ensure stability within the excavation area and safety for surrounding buildings, diaphragm walls are typically designed to penetrate significantly below the excavation face. The present design strategy often involves the use of buttress walls or cross walls to reduce lateral wall displacement and protect neighboring properties. This study focused on a large-scale deep excavation project on Liaoning Street, Chunghsiao Section, Taipei City, comparing numerical results with on-site measurements. The influence of different internal bracing removal timings on the lateral displacement of diaphragm walls was also explored.

1.1. Literature Review

In densely populated urban regions like Taipei, Shanghai, and Singapore, the necessity for underground space is inevitable. Over the past decades, the trend of utilizing subterranean spaces in urban developments, such as basements for parking and commercial

uses or subway systems, has been evident [1]. Deep excavation is typically employed for basement or cut-and-cover tunnel construction. In some instances, these excavations occur near existing subway tunnels or adjacent buildings [2–5]. Thus, the design and construction of deep pits should be meticulously executed to prevent excessive wall deflection, ground subsidence, or even wall collapses, as seen in cases like the Nicoll Highway failure [6]. Recent incidents, such as the substantial subsidence at the Dazhi Jitai construction site in Taipei in 2023, caused by inadequate ground improvement, ignorance of anomalous monitoring system alerts, and diaphragm wall damages, underline the profound impact of deep excavation construction on neighboring structures [7].

The literature review is organized into three main themes as shown in Tables 1–3.

Table 1. Literature Compilation Table on the Lateral Displacement of Diaphragm Wall.

Author	Abstract
Manna and Clough [8]	They utilized the finite element method to analyze factors influencing the deformation of excavation retaining walls. When comparing their findings with field observations from deep excavations, they identified several key influencing factors: the safety factor against uplift, stiffness of the retaining wall and support system, pre-stress magnitude of supports, plan geometry of the excavation area, and project duration.
Ou et al. [9]	They examined ten cases of deep excavation in the Taipei Basin where either pre-bored piles or diaphragm walls were employed. Their findings indicated that lateral displacements increased with excavation depth. The maximum lateral displacement (δh, max) ranged between 0.2% and 0.5% of the final excavation depth (He). Notably, in soft clays, the maximum displacement tends towards the upper limit, while in sandy grounds it leans towards the lower limit.
Clough and O'Rourke [10]	The patterns of retaining wall deformation due to excavation with internal struts and tie-backs can be categorized into cantilever displacement, deep inward displacement, and a combination of the two. Their analysis across different soil types—stiff clay, residual soil, and sand—revealed that the average maximum surface settlement was about 0.15 times the excavation depth. Cases with lateral displacement exceeding 0.5% of the excavation depth were attributed to construction malpractice or insufficient wall penetration.
Masuda et al. [11]	They categorized influential factors affecting excavation performance into two main groups based on an analysis of 52 excavation cases: soil stiffness and support stiffness. Furthermore, they summarized 11 reasons affecting retaining wall deformation, such as soil type, soil properties, wall stiffness, support quantity and spacing, pre-stress on supports, excavation method, wall length, ground improvement presence, scale of excavation, groundwater conditions, and other construction activities.
Wu et al. [12]	They consolidated data from Taipei's metro construction and past excavation projects in the city. Their results showed a relationship between the maximum lateral wall displacement (δ_{max}) and excavation depth (D) as δ_{max} = (0.07% to 0.2%) D. The depth at which this maximum displacement occurs, Za, was related to the excavation depth as Za = (0.8 to 1.2) D, averaging around the excavation depth.
Wang et al. [13]	They analyzed deep excavation cases in Kaohsiung's clay layer. Their findings suggested a relationship between the maximum lateral wall displacement ($\delta_{h,max}$) and the excavation depth (H) as $\delta_{h,max}$ = (0.1% to 0.4%) H.
Surarak et al. [14]	They back-calculated the Eu/Su ratio using the MC model, providing a reliable prediction for the lateral movement of retaining walls. However, this model was less successful in predicting surface settlements. Utilizing soil parameters from lab and field tests for both SSM (Small Strain Model) and HSM (Hardening Soil Model) analyses led to improved agreement with observed lateral wall movements and surface settlements.
Hsieh et al. [2]	They proposed a simplified method for predicting wall displacement and designing diaphragm walls to ensure safety standards are met. They used a three-dimensional numerical analysis to study the factors influencing wall displacement during excavation. These factors encompass excavation geometry, diaphragm wall thickness, wall spacing, wall penetration depth, diaphragm wall stiffness, strut axial stiffness, diaphragm wall axial stiffness, and undrained shear strength of clay.

Table 2. Literature Compilation Table on the Characteristics of Subsidence Induced by Deep Excavation.

Author	Abstract
Peck [15]	He compiled observational data on ground subsidence from excavation cases in areas such as Chicago and Oslo, proposing a relationship between ground subsidence (δ_v) and distance from the retaining wall (d).
Ou and colleagues [9,16,17]	They delineated that subsidence from deep excavation generally exhibits two patterns: triangular trough and concave trough.
Wang et al. [13]	They analyzed deep excavation cases in Kaohsiung, concluding that the relationship between maximum ground subsidence and excavation depth is approximately $\delta_{v,max}$ = (0.04–0.25%)*He*, where *He* is excavation depth and $\delta_{v,max}$ = (0.21–1.10) $\delta_{v,max}$ for maximum wall displacement.
Avanti [18]	He observed that the finite element analysis of ground subsidence in the Jakarta Metro project shows an arch-shoulder type. Larger R_{inter} values (as a parameter to represent interfaces between soil and structure) lead to a concave trough type of ground subsidence, which accurately predicts building damage, as illustrated in Figure 1a. If the subsidence is of the concave type, taking the TNEC (Taipei National Enterprise Center) case as an example (Ou [19]), it can be discerned from the ground subsidence contour that Building A has tilted and begun to sink during excavation, as shown in Figure 1b.

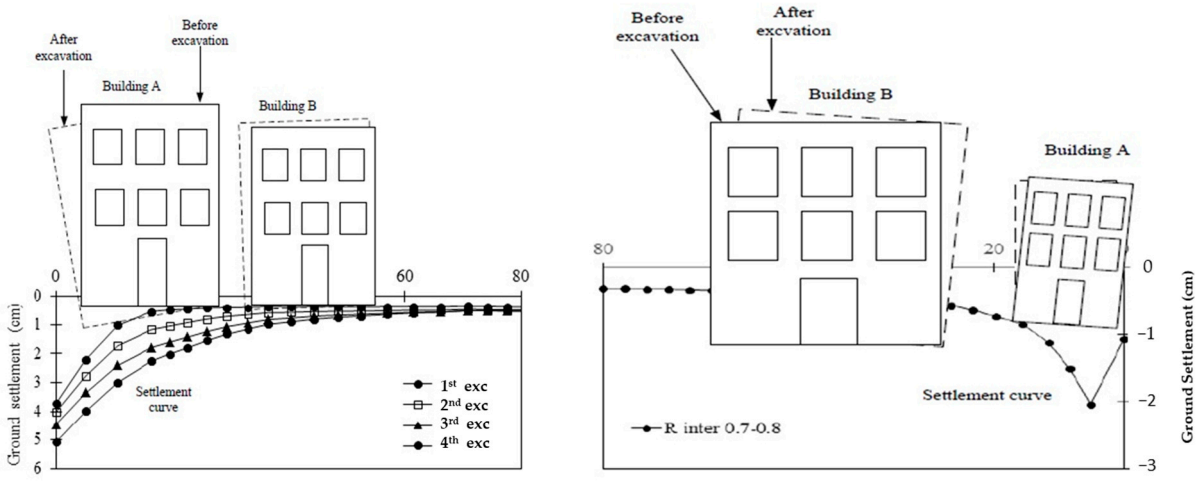

(**a**) (**b**)

Figure 1. (**a**) Predicted Arch-Shoulder Surface Settlement after Deep Excavation in Jakarta Metro Project; (**b**) Predicted Building Tilt Post Deep Excavation in the TNEC Case Study.

Table 3. Literature Compilation Table on the Application of Numerical Analysis in Deep Excavation Engineering.

Author	Abstract
Liao [20], Wang [21] and Hsieh [22]	They utilized numerical analysis to study the behavior of wall deformation and ground subsidence in Taipei's deep excavation projects. The results indicated a significant underestimation of maximum ground subsidence ($\delta_{v,max}$), which often appeared further from the retaining wall than the actual observations. This led to overestimations in secondary affected areas, and unconverged values at the end of these regions. The primary reason for these discrepancies was that the existing analysis could not smoothly simulate the small strain behavior of the soil.
Hsieh [23] and others	They pointed out that three-dimensional numerical analysis simulating excavations in Taipei with central walls and struts compared well with monitoring data.
Chen et al. [24]	They used a 3D software tool to study the effect of exterior struts in reducing the maximum lateral deformation in the middle of the Diaphragm Wall.
Khoiri and Ou [25]	They explored wall displacement and ground subsidence for the Kaohsiung Metro System O6 station using both MC (Mohr-Coulomb Model) and HS (Hardening Soil Model).

Table 3. *Cont.*

Author	Abstract
Ou et al. [26]	They showed that installing a central wall can reduce the maximum wall deformation by 75% and maximum ground subsidence by 82%. They discussed the corner effects of retaining walls using a 3D numerical method.
Ye [27]	They used PLAXIS 3D Foundation to simulate a real project, suggesting that central walls and struts can significantly enhance the stiffness of the Diaphragm Wall.
Feng [28]	They employed the "Plaxis 3D" software to study the effects of different spacings, thicknesses, and penetration depths for struts and central walls, emphasizing their effectiveness in reducing lateral wall movement and ground subsidence.

1.2. Introduction to Buttress Walls, Cross Walls, and Wall Piles

With the increasing depth of excavations in recent constructions, retaining walls are subjected to immense hydrostatic pressures, posing significant construction risks. Insufficient rigidity of diaphragm walls, inadequate lateral support, construction flaws leading to prestress losses, or excessive base size can result in considerable lateral displacement of these walls. When excavations are conducted in soft clay layers, the low elastic modulus and strength of the soil can cause substantial displacement of the diaphragm wall and excessive ground settlement, leading to potential damage to adjacent properties. Nevertheless, recent research and case studies have demonstrated that the implementation of buttress Walls and in-ground walls can effectively enhance the rigidity of diaphragm walls, reduce their displacement, and ground settlement, and provide resistance against uplift forces.

1. Internal Buttress Walls: Positioned on the excavation side of the diaphragm wall, these walls primarily serve to enhance the wall's rigidity, curbing deformations due to excavation-induced decompression. They are progressively removed as excavation proceeds and can be regarded as a temporary support system.
2. External Buttress Walls: Located on the non-excavated side of the diaphragm wall, external Buttress Walls differ from their internal counterparts. They are seen as an integral part of the diaphragm wall structure and are usually reinforced. Their primary function is to increase the rigidity of the diaphragm wall. Unlike internal walls, they are not removed during excavation phases.
3. Cross Walls: These walls are set up to connect the Diaphragm Wall on either the north-south or east-west sides and can be seen as a support system. They offer significant rigidity to the diaphragm walls, effectively limiting wall deformation, differential foundation settlement, and providing resistance against uplift. They are generally reinforced below the excavation face and are removed progressively with excavation.
4. Wall Piles: A subset of foundation piles, wall piles play a vital role in preventing uplift, enhancing foundational load-bearing capacity, and minimizing differential settlement.

2. Materials and Methods

2.1. Research Methodology and Steps

The behavior of retaining walls during foundational excavation and its subsequent impact on the surrounding ground surface has been the subject of numerous studies. The most commonly utilized one-dimensional retaining wall analysis software in the industry is the RIDO program developed by Robert Fages Logiciels and the TORSA program devised by the Geotechnical Technology Research Development Foundation. Moreover, two-dimensional and even three-dimensional numerical analysis software are employed for simulation reviews. This research relied on the excavation data from the "Taipei Liaoning Street Changchun Section New Construction Project" and employed the finite element method via the PLAXIS 3D 2018 software for simulation. The results from the simulation were then juxtaposed against onsite monitoring data to validate the accuracy of soil and structural parameters, as well as the chosen soil constitutive laws. Prior studies have shown that the timing of removal for Buttress Walls and cross walls can influence wall

displacement and ground settlement. Hence, this study investigated the efficiency of displacement reduction in retaining walls by varying the timing of strut and in-ground wall removals. The procedural layout for this research is illustrated in Figure 2.

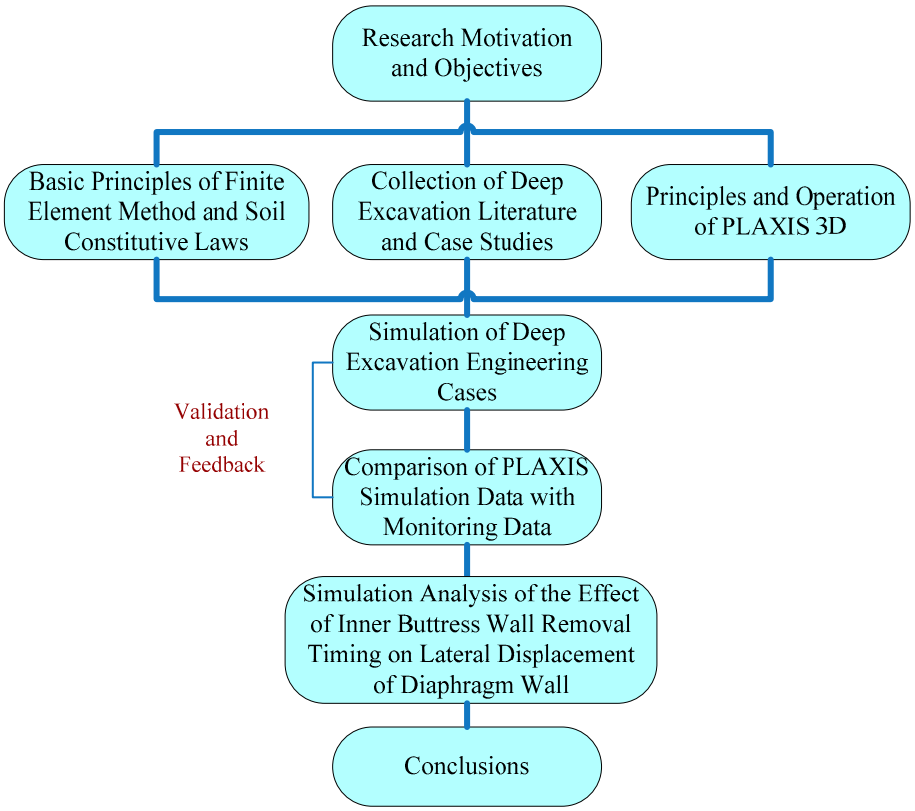

Figure 2. Research Process Diagram.

2.2. Research Content

- Validation of PLAXIS Numerical Analysis Simulation and Monitoring Data

An introduction to the PLAXIS numerical analysis software, which encompasses the theory of the finite element method, the constitution laws of soil materials, an overview of different soil models within Plaxis 3D, and the usage of related parameters.

- Simulation Analysis of the Timing for Internal Buttress Wall Removal

Analysis of the timing for the removal of buttress Walls and cross walls. By altering the removal timings, the study aimed to discern its influence on wall displacement.

2.3. Numerical Simulation

(1) Software Overview

PLAXIS is a finite element analysis software, due to its ability to easily tackle a plethora of geotechnical engineering problems and its intuitive graphical user interface, its adoption has progressively increased in both academic and professional sectors. The version adopted for this research is PLAIXS 3D 2018.

Plaxis 3D is adept at simulating the deformation and stability of complex geotechnical engineering tasks, such as large-scale foundation excavation and its mutual influence with surrounding environments, shield tunnel construction's interaction with neighboring structures, pile foundations, etc. Its features include:

- Simulation capabilities encompassing: elements, soil bodies, various elements and soil body interfaces, wall, plate, beam structures, pile foundations, braces and anchors, tunnels, and groundwater seepage analysis.

- Analytical capability for deformation, consolidation, graded loading, stability, and seepage, as well as variations in shear, bending moment, and axial stress for various structures, hydrosols, and temporary support elements. It can also consider the impact of low-frequency seismic loads.
- In terms of soil material stress-strain constitutive models, it offers:
  1. Linear-elasticity model.
  2. Mohr-Coulomb model.
  3. Soft Soil Creep Model.
  4. Hardening Soil Model.
  5. Hardening Soil Model with Small-strain.

(2) Hardening Soil Model

- Principles

In this study, we predominantly used the Hardening Soil model (HS) from the five soil material constitutive laws embedded within the Plaxis 3D software. The HS model is an advanced soil model capable of simulating behaviors of both soft and hard soils. This model adopts the Mohr-Coulomb failure criterion and employs plasticity theory, making its stress-strain behavior more aligned with the real-world soil responses than the conventional Mohr-Coulomb. As illustrated in Figure 3a, while an idealized soil model exhibits a linear-elastic perfect plastic behavior, the actual stress-strain relationship of soil is nonlinear. The HS model offers a closer approximation to this real-world stress-strain relationship. Furthermore, the HS model incorporates the shear dilation of the soil and features a yield cap, facilitating a more realistic simulation of soil behaviors.

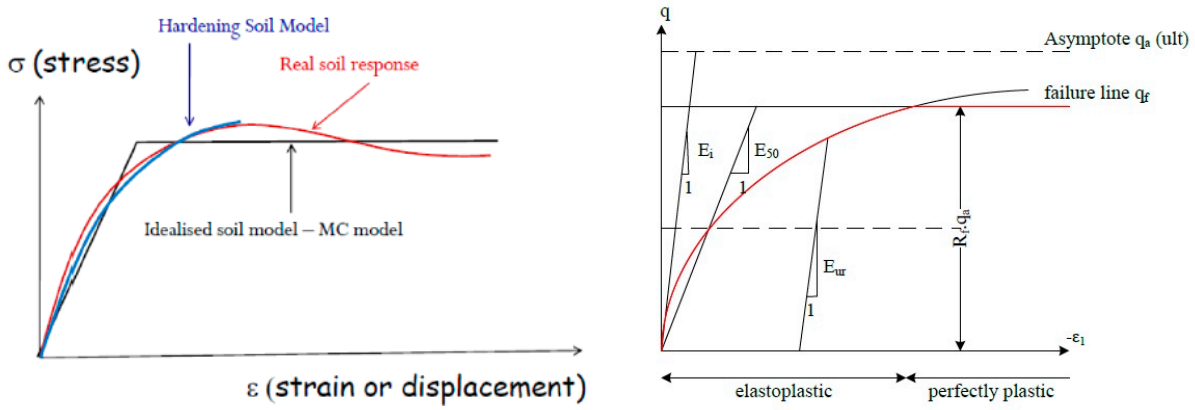

Figure 3. (**a**) The HS model more closely resembles real-world soil behavior; (**b**). Stress-strain relationship in the soil hardening model.

The HS model can simulate the nonlinear stress-strain relationship of soils, meaning that the stiffness at each stress level (Stress-Level) varies during the loading process. As depicted in Figure 3b, when observed through drained triaxial tests, the stress-strain exhibits a hyperbolic relationship:

$$\text{axial strain}: -\varepsilon_1 = \frac{1}{2E_{50}} \times \frac{q}{1 - \frac{q}{q_a}} \quad (1)$$

Here, q denotes axial stress, q_a is the shear strength asymptote, and q_f is the stress value corresponding to the asymptote of the hyperbola (stress-strain relationship). E_i represents the initial modulus of elasticity.

When q < q_f, $R_f = \frac{q_f}{q_a}$, and Equation (1) can be rewritten as $E_i = \frac{2E_{50}}{2-R_f}$. The stiffness modulus of the confining stress under the main load can be found using Equation (1):

$$E_{50} = E_{50}^{ref}\left(\frac{c\cdot cos\varphi - \sigma_3\prime\cdot sin\varphi}{c\cdot cos\varphi + P^{ref}\cdot sin\varphi}\right)^m \quad (2)$$

Here, P_{ref} signifies the reference pressure (set internally at 100 kN/m^2), E_{50}^{ref} is the secant modulus of elasticity at 50% limit strength under the reference pressure, $\sigma_3{}'$ is the lateral effective stress, φ is the internal friction angle, and m is the exponent for the modulus of elasticity concerning stress.

Not only can the HS Model simulate nonlinear stress-strain relationships, but by utilizing plasticity theory, it can also compute the plastic strain amount at each stress stage. Additionally, plastic strains commence from the initial stages of loading. Moreover, its yielding criterion not only encompasses the yield surface caused by axial differential stress but also contemplates the yield surface induced by confining stress.

- Input Parameters for the HS Model

  1. General Parameters

     Saturated unit weight γ_{sat} and unsaturated unit weight γ_{unsat} (kN/m^3), along with the porosity ratio e.

  2. Stiffness Parameters

     E_{50}^{ref}: Triaxial drained secant modulus under reference stress.
     E_{oed}^{ref}: One-dimensional oedometric secant modulus under reference stress.
     E_{ur}^{ref}: Modulus of elasticity for loading-unloading under reference stress.
     m: Power for the relation between elastic modulus and stress.

  3. Strength Parameters

     C_{ref}: Effective cohesion
     φ: Effective friction angle (deg)
     Ψ: Dilation angle (deg)

  4. Advanced Strength Parameters

     ν_{ur}: Poisson's ratio for unloading-reloading. By default in the PLAXIS 3D manual, it is 0.2.
     p^{ref}: Reference stress. According to the PLAXIS 3D manual, the default is 100 stress units.
     R_f : Failure ratio. By default in the PLAXIS 3D manual, it is set to 0.9.
     $\sigma_{tension}$: Tensile strength. The default value is 0 (kN/m^2).

2.4. Parameter Settings for Soil Layer Drainage Conditions

- Drained Conditions

Primarily simulates drainage or long-term loading behavior. Both the stiffness and strength parameters input are based on effective values.

- Undrained (*A*) Parameters

This is mainly for simulating short-term behaviors under undrained or loading conditions. A high bulk modulus of water is applied to render the soil incompressible. The undrained (*A*) computation is based on undrained effective stresses, and both stiffness and strength parameters input are effective values. Pore water pressure (including excess pore water pressure) is computed, with accuracy dependent on the chosen model and parameters.

- Undrained (*B*) Parameters

Similar to the undrained (*A*) condition, this simulates short-term behaviors under undrained or loading situations. The soil is rendered incompressible using a high bulk modulus of water. The undrained (*B*) computation is conducted based on undrained effective stresses, where stiffness parameters are based on effective values while strength parameters utilize undrained shear strength. Pore water pressure (including excess pore water pressure) is computed, but results might be significantly imprecise.

- Undrained (*C*) Parameters

This is for modeling short-term behaviors under undrained or loading conditions. Both stiffness and strength parameters are based on total stress values. The stiffness is simulated using the elastic modulus (E_u) and the undrained Poisson's ratio (ν_u). The strength is modeled using the undrained shear strength (S_u) and friction angle (ϕ_u). Note, that if an undrained Poisson's ratio (ν_u) of 0.5 is chosen, the software cannot compute it; thus, an input value of 0.495 should be used. This mode does not compute excess pore water pressure.

- Non-Porous Condition

  No pore water pressure is generated.

2.5. Model Creation Process

The procedure for establishing a model in PLAXIS 3D for deep excavation projects is as follows. (For a detailed explanation, please refer to the software user manual).

1. Define the overall boundary profile of the model.
2. Specify the soil parameters.
3. Structure simulation.
4. Adjacent building load simulation.
5. Define construction steps and water level settings.
6. Specify the mesh and mesh density.

2.6. Model Limitations

PLAXIS is a finite element software used for geotechnical and soil-structure interaction analysis. While it is highly robust and versatile, like any software, it has its limitations. Here are some of the constraints related to the maximum allowable limits when using PLAXIS for modeling:

- Element Number Limitations:
  - Complexity: PLAXIS has a limit on the number of elements that can be modeled. For highly complex structures or extensive geotechnical scenarios, this could be a limiting factor.
  - Computational Efficiency: More elements mean longer computation times and more intensive use of computer resources.
- Material Properties:
  - Accuracy: There are limits in modeling the exact material properties, especially for heterogeneous soil conditions or complex materials.
  - Non-linearity: Although PLAXIS can handle non-linear materials, there can be complexities and limitations in extreme scenarios.
- Boundary Conditions:
  - Flexibility: While PLAXIS offers a range of options for setting boundary conditions, in some specialized or extreme cases, the options might not be adequate.
  - Real-World Representations: Representing real-world boundary conditions accurately can sometimes be challenging.
- Loading Conditions:
  - Dynamic Loads: There might be limitations in simulating certain types of dynamic or cyclic loading conditions.

  - Extreme Loads: While PLAXIS is capable of simulating a variety of load types, extreme loading scenarios can sometimes push beyond its capabilities.
- Analysis Types:
  - Consolidation Analysis: PLAXIS has certain constraints in dealing with very long-term consolidation and creep analysis.
  - Environmental Factors: The simulation of some specific environmental influences might be constrained.
- Software and Hardware Interaction:
  - Hardware Limitations: The performance of PLAXIS is also dependent on the hardware on which it is run. Hence, limitations in hardware can impact the efficiency and speed of analysis.
  - Parallel Processing: There could be limitations in the efficiency of parallel processing for very large models or complex analyses.

In using PLAXIS, engineers and researchers need to be mindful of these limitations and consider augmenting their analyses with additional tools, testing, or modeling approaches where necessary to ensure comprehensive and accurate results. Always refer to the latest manuals and technical documents of PLAXIS for the most updated and specific details on its capabilities and constraints.

3. Numerical Simulation and Monitoring Data Validation

In this chapter, the results from the numerical analysis of deep excavation projects using PLAXIS 3D 2018 were compared with actual monitored values. Real-world project data, including drilling reports, soil experiment parameters, site geometry, support structure configurations, construction processes, etc., were taken into consideration. The closer the simulation was to real-world conditions, the better. Later, the simulation results were juxtaposed with on-site monitoring data to verify if assumptions about soil parameters, structural parameters, model geometric conditions, construction, dewatering steps, and neighboring building loads are consistent with actual conditions. This will serve as the basis for future analyses on the timing of bracing and diaphragm wall removal.

3.1. Case Overview

The real-world project selected for this study is located in Liaoning Street, Zhongshan District, Taipei City. The site, roughly rectangular, covers an area of 9081 m^2. The original site was a flat parking lot. To the east, it is closely bordered by two-story, three-story, and six-story neighboring buildings. On the west side, the site faces Liaoning Street, which is 11 m wide, with a park located across the street. The northern edge of the site also borders an 11-m wide Liaoning Street (Lane 185), with another park situated across this lane. To the south, the site is bounded by an 8-m wide Liaoning Street (Lane 155), beyond which lie a three-story building and two larger buildings of 14 and 11 stories with 3 and 1 basement levels respectively. The plan was to construct a building with twenty floors above ground and six underground. The main excavation area measured approximately 98.0 m to the south, 80.0 m to the north, and 52.4 m for both the east and west sides, resulting in an excavation area of around 1900 square meters. The site layout is shown in Figure 4. According to structural design data, the excavation depth at this site was 25.7 m. The diaphragm wall, used as a retaining measure, was 54 m deep on the south side, and 52 m on the other three sides, with a thickness of 1.2 m throughout. The top-down construction method was adopted. To mitigate potential wall displacement and surface subsidence for the safety of neighboring properties, three diaphragm walls oriented north-south, each 60 cm thick, were placed within the excavation area. Additionally, on both the north and south sides, there were eight bracings, each 10 m long and 60 cm thick. Both the east and west sides had four bracings, each 12 m long and 60 cm thick. Horizontal bracing was positioned at a depth of 21.8 m.

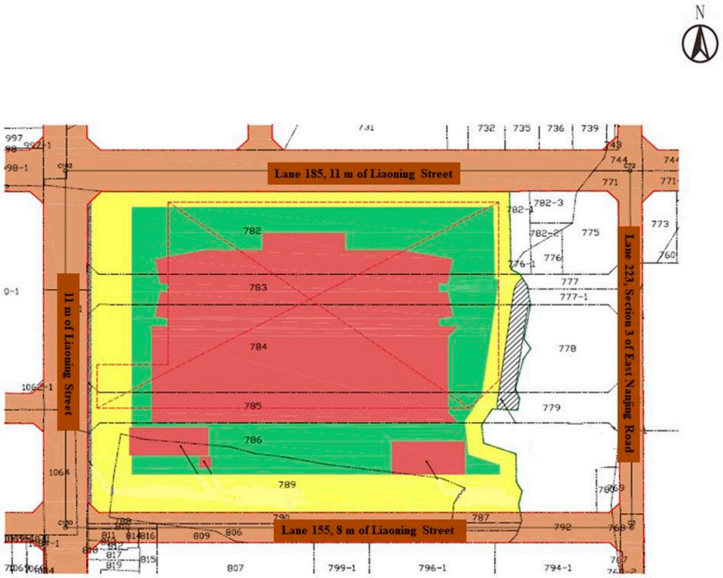

Figure 4. Site Location Map.

(1) Stratigraphy Overview

Based on the on-site drilling investigation report, the drilling depth of this study reached 62.0 m, broadly divided into seven strata, alternating between clay and sandy layers. The groundwater level during drilling was found to be approximately GL-2.8 m. A concise soil layer description table from the drilling report is provided in Table 4 (For additional details, please refer to Supplementary Table S1, with a sectional view of the soil layers presented in Supplementary Figure S1.

Table 4. Concise Soil Layer Description Table.

Layer	Soil Layer Description	Layer Bottom Distribution Depth (GL.−m)	Average Distribution Elevation (GL.−m)
1	Backfill Layer (SF)	0.1~0.9 (0.5)	0.0~0.5
2	Silty Clay Layer (CL)	1.8~3.7 (3.0)	0.5~3.0
3	Silty Sand Layer (SM)	9.2~10.6 (9.9)	3.0~9.9
4	Silty Clay Layer (CL)	19.8~27.4 (23.1)	9.9~23.1
		40.0~41.5 (40.7)	23.1~40.7
5	Silty Sand Layer (SM)	40.9~45.0 (42.2)	40.7~42.2
6	Silty Clay Layer (CL)	51.9~54.3 (52.7)	42.2~54.7
7	Gravel Layer (GW/GP)	- (Drilling Depth)	>52.7

(2) Diaphragm Wall, Buttress Wall, and Cross Wall Overview

For this study, the excavation depth was 25.7 m and a 1.2-m thick diaphragm wall served as the retaining measure. Both the east and west sides had four bracings, each 12 m long and 60 cm thick, as depicted in Figure 5. These temporary installations, the buttress and diaphragm walls, were designed to control excessive displacement of the diaphragm wall and were removed sequentially during the excavation process. For deeper excavation levels, especially for the raft foundation level, horizontal bracing was positioned at a depth of 21.8 m to prevent excessive wall displacement.

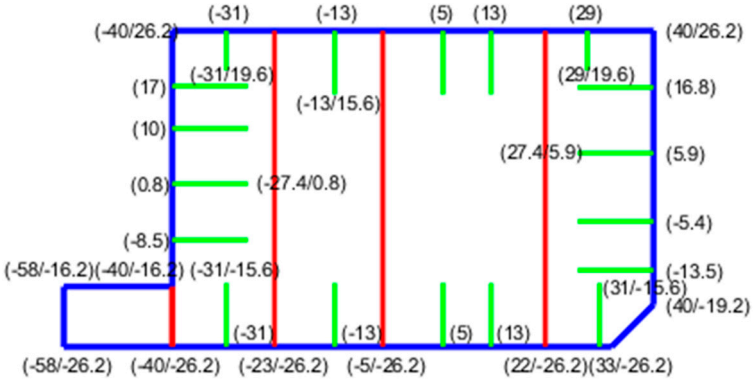

Figure 5. Diagram illustrating the colored positions of each wall. (where, the blue line represents diaphragm wall, the green line represents buttress wall, and the red line represents cross wall).

(3) Overview of the Top-down Construction Method

For this case, with an excavation depth of 25.7 m, the top-down construction method, also known as the reversed construction method, was employed. Before excavation, a diaphragm wall is erected around the excavation area of the site. Coupled with the foundation pile construction, steel columns (also known as internal columns) are suspended to bear the load. Once these structures have cured, excavation and floor slab construction proceed sequentially from the surface downwards. As each level's excavation is completed, the slab for that level is constructed. Upon reaching the required strength, excavation and slab construction for the subsequent level begin, continuing in this manner until the desired depth is achieved. Concurrently, the above-ground structure is built as per design load specifications. This method differs from the conventional open-cut with shoring, minimizing issues like wall displacement and surface subsidence during deep excavation. It is particularly suited for urban construction or underground projects like subways and metros. The floor slabs in the underground structure also serve as internal shoring but are stiffer than traditional steel shoring, thereby enhancing safety during excavation operations. However, during the final excavation to the lowest level, the raft foundation and the lowest floor are excavated at once. To prevent excessive wall displacement due to the removal of the floor slab's supporting effect, horizontal bracing is installed at a depth of 21.8 m. This method's illustration is presented in Figures 6 and 7.

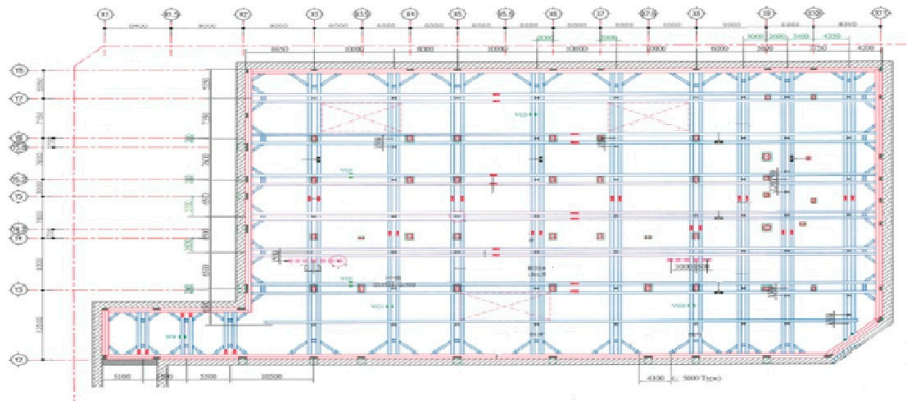

Figure 6. Plan Layout of Excavation Base Support.

(4) Introduction to the Monitoring System

Although this engineering case has established methodologies and measures for stable excavation, there are local variations within the site that cannot be fully understood with limited borehole data. Moreover, the analytical theory applied is still based on accumulated empirical formulas. Concurrently, unforeseeable factors during the construction process

could potentially impact the work. Hence, to ensure the safety of the basement excavation, adjacent buildings, surrounding roads, and public facilities, it is imperative to install a safety monitoring system both inside and outside the site during construction. The data obtained during construction should be organized, interpreted, and analyzed to verify the safety of each excavation stage and to predict potential situations in each construction phase. If necessary, mitigation measures should be taken in advance to prevent disasters. The layout of the monitoring system for this case study is shown in Figure 8.

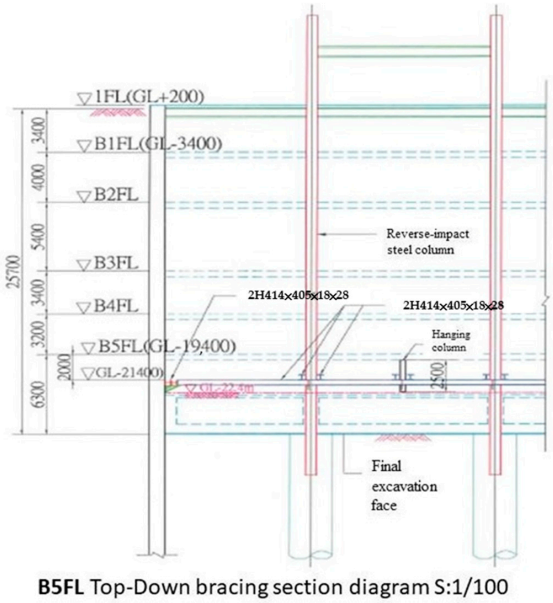

Figure 7. Cross-sectional Schematic of Excavation Base Support at depth of 21.8 m.

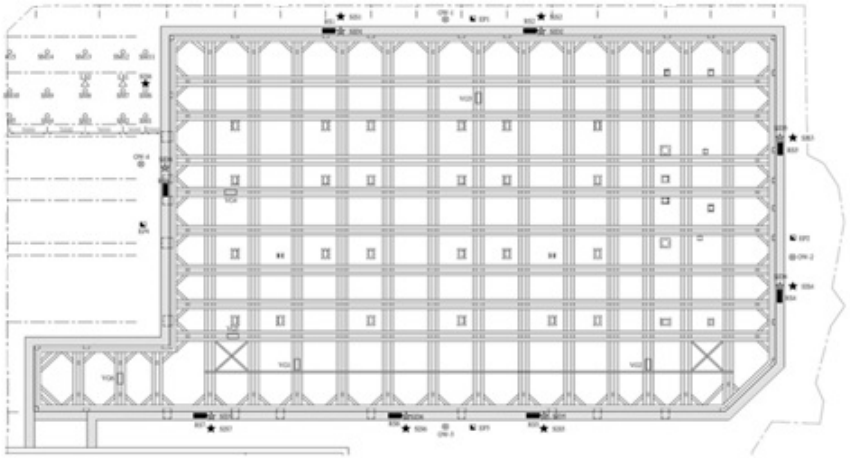

Item	Monitoring item	Symbol	No	Quantity	Instrument name
1	Lateral displacement of diaphragm wall	☆	SID	8	Inner Wall Inclination Meter
2	Lateral displacement of geological strata	★	SIS	8	Outer Wall Inclination Meter
3	Steel reinforcement stress	▬	RS	8	Reinforcement Stress Gauge
4	Support stress	▭	VG	6	Strut Strain Gauge
5	Groundwater level	⊗	OW	4	Water Level Observation Well
6	Groundwater pressure	◪	EP	4	Electronic Hydraulic Pressure Gauge*4
7	Top-down steel column settlement point	_	RHE	20	Settlement Scale
8	Surface settlement	○	SM/SB	-	Ground Settlement Monitoring Point
9	Building inclination	-	-	-	Building Inclinometer
10	Strata settlement	△	LS	2	Multi-Point Extensometer

Figure 8. Layout of the Monitoring System Plan.

Additionally, the monitoring frequency often varies due to factors such as project scale, site geological conditions, chosen construction methods, construction sequence, construction techniques, and construction duration. Therefore, it is essential to adjust based on on-site conditions, providing ample data for analytical interpretation (serving the function of hazard early warning), and establishing the principle for determining monitoring frequency.

3.2. Case Study Simulation

(1) Model Geometry

This research employed the three-dimensional finite element method software PLAXIS 3D 2018 for numerical simulation. The soil element mesh consisted of tetrahedral elements with 10 nodes. The excavation site chosen was somewhat rectangular in shape, with a small chamfer on the southeast side and a protruding rectangle on the southwest. This model adopted a full-section analysis. According to the study by Heish and Ou [29], the ground subsidence caused by deep excavation, whether triangular or trough-shaped, primarily affects the area within a distance of twice the excavation depth from the diaphragm wall. Moreover, the primary influence zone is approximately equivalent to the secondary influence zone (where the surface subsidence area comprises the primary influence zone (PIZ) and the secondary influence zone (SIZ)). The former exhibits a larger subsidence magnitude and a wider affected area, characterized by a steeper subsidence curve. In contrast, the latter has a smaller subsidence magnitude and a more limited affected area, featuring a gentler subsidence curve. Consequently, during excavation, surface subsidence is primarily governed by the PIZ, with an approximate range extending up to twice the excavation depth). Therefore, during analysis, selecting four times the excavation depth adequately captured the subsidence range affected by excavation. Since this research took into account the effects of neighboring buildings and road loads during simulation, a distance of five times the excavation depth from the diaphragm wall was set as the model's horizontal boundary (in the X and Y directions). The model extended vertically into the cobblestone layer, with a mesh depth (in the Z direction) of 62.0 m. In summary, the overall model boundary dimensions were 260 m × 240 m × 62 m. The mesh boundary conditions were set with hinge supports at the base boundary and roller supports at the peripheral boundaries. The model geometry is depicted in Figure 9.

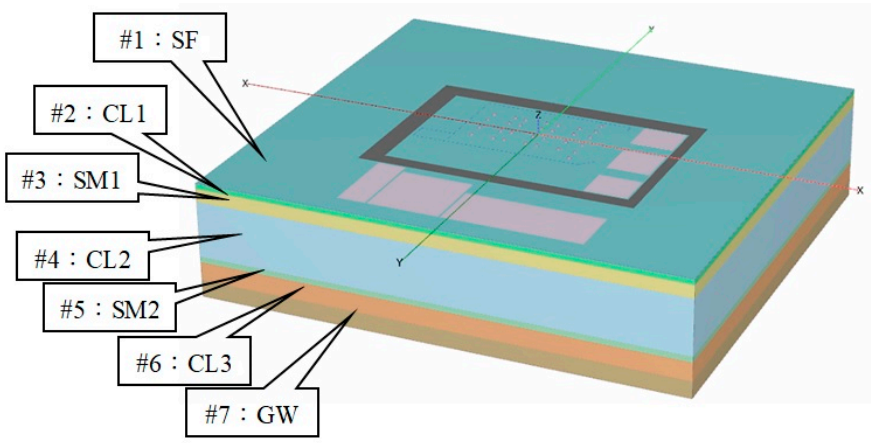

Figure 9. Geometry and Stratum Construction of the PLAXIS 3D Model.

(2) Initial Soil Stress

Based on the study by Heish [2], the silt clay in Taipei, under regular compaction, at-rest earth pressure coefficient closely approximates Equation (3). Therefore, when considering clay, Equation (4) can also be adopted. While accounting for the over-consolidation

behavior of clay, Equation (4) is first used to calculate k_0, and then, as suggested by Ladd [30], Equation (5) is employed to estimate $k_{0,OC}$:

$$k_0 = 1 - sin\phi' \tag{3}$$

$$k_{0,NC} = 1 - sin\phi' \tag{4}$$

$$k_{0,OC} = k_0(OCR)^{\alpha} \tag{5}$$

where, $k_{0,OC}$ = static earth pressure coefficient of over-consolidated soil, α = empirical coefficient (for PI = 20, α = 0.4; for PI = 40, α = 0.32)

(3) Soil Parameter Selection

This study's case was situated in the Taipei Basin and comprised seven soil layers. The first layer was a backfill layer, while the third and fifth layers were sandy soil layers. The second, fourth, and sixth layers were clay layers, with the bottommost seventh layer being a gravel layer. The soil layer setting depth is aligned with a geological drilling depth of 62 m. The numerical model's soil layer setup is illustrated in Figure 9.

For both sandy and clayey soils, this research employed the Hardening Soil Model for analysis. Fundamental parameters required for the analysis with the Hardening Soil Model include γ_t, e, c, ϕ, ν, stiffness parameters E_{50}^{ref}, E_{oed}^{ref}, E_{ur}^{ref}, permeability coefficients, drainage properties, and more. The following provides a sequential introduction to the bases of their selections (see Tables 5–7).

Table 5. Soil Parameter Input for the Layers in This Study.

Modulus	Clay	Sand
Soil Unloading Elastic Modulus	$E_{ur}^{ref} = \frac{3(1+e)p^{ref}(1-2\nu_{ur})}{Cs/2.303}$	$E_{ur}^{ref} = 3E_{50}^{ref}$
Soil Shear Elastic Modulus	$E_{50}^{ref} = 1/3E_{ur}^{ref}$	$E_{50} = E_{50}^{ref}\left\{\frac{c\prime\cos\varnothing' - \sigma_3\prime\sin\varnothing\prime}{c\prime\cos\varnothing' + p^{ref}\sin\varnothing\prime}\right\}$
Soil Bulk Elastic Modulus	$E_{oed}^{ref} = 0.8E_{50}^{ref}$	$E_{oed}^{ref} = E_{50}^{ref}$

Table 6. Poisson's Ratios for Different Soils (Ou [31]).

Soil Type	Poisson's Ratio ν
Saturated Clay (Undrained)	0.5
Unsaturated Clay (Undrained)	0.35–0.4
Silty Sandy Clay	0.3–0.4
Silty Sand	0.3–0.4
Sand and Gravel Soil	0.15–0.35
Silt Soil	0.3–0.35
Rock	0.1–0.4 (varies by type)
Concrete	0.15

(4) Setting of Neighboring Building and Road Load Parameters

The case study under consideration was surrounded by neighboring buildings and roads. To accurately simulate the actual on-site conditions, it was essential to consider the loads from neighboring buildings and road surfaces when assessing the impact of excavation on the site. Therefore, prior to the excavation simulation, the loads from the surrounding buildings and roads were applied directly to the ground surface using a surface load approach. This method simplified the analysis and accelerated the computation speed. The parameters related to neighboring structures are presented in Table 8, and the 3D model configuration of the neighboring buildings is illustrated in Figure 10.

Table 7. Soil Material Parameter Table.

Item No.	Soil Layer	Depth (m)	γ_{unsat} (kN/m^3)	γ_{sat} (kN/m^3)	c' (kN/m^2)	φ' (°)	E_{50}^{ref} (kN/m^2)	E_{oed}^{ref} (kN/m^2)	E_{ur}^{ref} (kN/m^2)	ν_{ur}	ψ	m
#1	SF	−0.5	19.1	19.6	0.5	30	20,000	20,000	60,000	0.20	0	0.5
#2	CL1	−3.0	19.0	19.3	0.7	29	9000	7200	27,000	0.20	0	1.0
#3	SM1	−10.0	19.5	20.1	0.7	30	28,000	28,000	84,000	0.20	0	0.5
#4	CL2	−40.0	18.8	19.0	1.1	30	17,000	13,600	51,000	0.20	0	1.0
#5	SM2	−43.0	19.0	19.5	1.0	31	34,500	34,500	103,500	0.20	1.0	0.5
#6	CL3	−53.0	19.2	19.5	1.5	31	19,000	15,200	57,000	0.20	1.0	1.0
#7	GW	−62.0	21.5	21.7	1.0	35	70,000	70,000	210,000	0.20	5.0	0.5

Soil Parameter	Soil Parameter Selection Description
Drainage Properties	According to the PLAXIS manual, a model's drainage behavior can be categorized into drained, undrained A, undrained B, undrained C, and impervious scenarios. Given that sandy soil quickly expels excess pore water pressure due to its larger voids, effective stress analysis with drainage behavior is utilized. Clay sections are modeled with undrained behavior, and for analysis consistency with sandy soil, the undrained A scenario is chosen. Undrained A uses effective stiffness and strength parameters to simulate undrained behavior.
Wet Soil Unit Weight γ_t, Effective Cohesion c', Effective Friction Angle ϕ'	Values for wet soil unit weight, effective cohesion, and effective friction angle can be derived from drilling reports and laboratory tests. The PLAXIS manual suggests inputting a slightly larger value when effective cohesion is 0 to speed up analysis.
Void Ratio e, Specific Gravity Gs	The soil parameter table in this study did not provide specific gravity and void ratio data. Following recommendations from Ou's "Deep Excavation Engineering Analysis, Design Theory, and Practice", an assumption was made that each soil layer has a specific gravity of 2.7 [31]. The void ratio was then inferred using the saturated unit weight and specific gravity.
Soil Elastic Modulus Es	Attention is crucial when analyzing sandy soil in deep excavation projects. Based on research by Ou et al. [26], the effective internal friction angle reflects the friction between soil particles, related to the roughness, shape, and compression of the soil particles. The elastic modulus is associated with the physical properties and inter-particle forces. In practice, empirical formulas often estimate these. In this research, the soil layers utilized the Hardening Soil Model, with the soil parameters summarized in Table 5. According to Khoiri and Ou [25], the recommended elastic modulus Es for sandy soil using the HS model ranges from Es = 2000–4000 N. This study adopts Es = 3000 N.
Permeability Coefficient K	Based on Ou [31], various soil types' permeability coefficients have been collated. This study adopted the permeability coefficients for Taipei silty clay K = $(0.5 - 2.0) \times 10^{-7}$ cm/s and Taipei silty sand K = $(0.5 - 6.0) \times 10^{-4}$ cm/s.
Poisson's Ratio ν	Ou [31] provided ranges for the Poisson's ratio of various soils, as shown in Table 6.
Other Relevant Parameters	The parameters obtained from empirical formulas, drilling reports, and laboratory experiments are listed in Table 7.

Note: The PLAXIS manual recommends a soil parameter $c' \geq 0.2$ kN/m^2 to prevent convergence issues during analysis.

Table 8. Parameters of Neighboring Structures.

Item	Material Type	Thickness t (m)	Distribution Depth d (m)	Unit Weight r (kN/m^3)	Modulus of Elasticity E (kN/m^2)	Poisson's Ratio ν′
2F Neighbor	Plate	1.0	0	20.0	2.1×10^7	0.15
3F Neighbor	Plate	1.3	0	30.0	2.1×10^7	0.15
6F Neighbor	Plate	2.1	0	50.0	2.1×10^7	0.15
11F Neighbor	Plate	3.1	0	90.0	2.1×10^7	0.15
14F Neighbor	Plate	3.8	0	100.0	2.1×10^7	0.15
Road				5.0	9.81	0.15

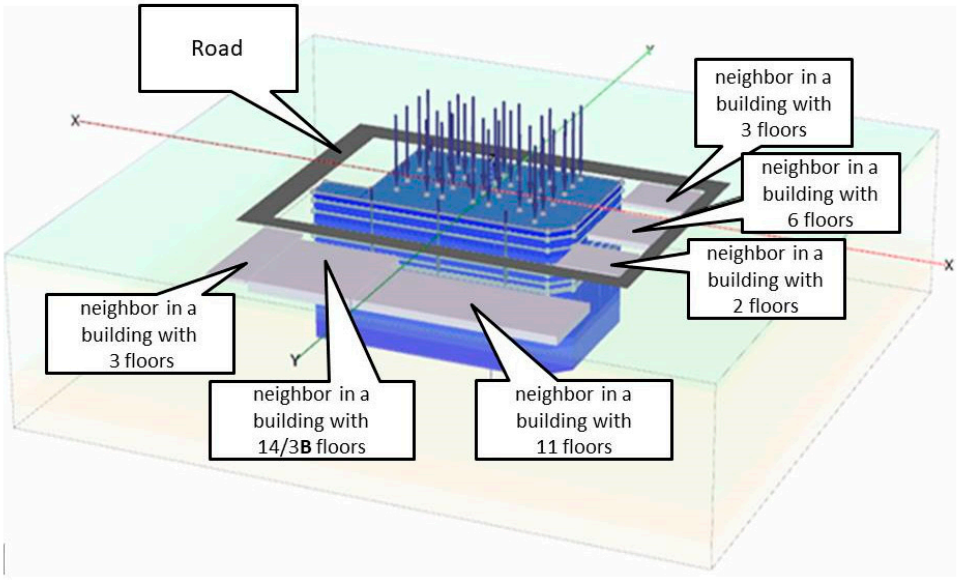

Figure 10. Configuration of neighboring buildings in the PLAXIS 3D model.

The estimated load per square meter for each floor of the neighboring buildings was derived from Taiwan's Building Technical Regulations for Building Structures. The static load was approximated as 550 kgf/m^2 (D $\approx$ 2400 kgf/m^3 $\times$ 0.2 + 70 kgf/m^2), and the live load for residences was roughly L $\approx$ 200 kgf/m^2. Based on the safety factors stipulated in the Reinforced Concrete Design Code, the estimated load for each floor of the neighboring buildings was calculated as 980 kgf/m^2 (1.2 $\times$ 550 kgf/m^2 + 1.6 $\times$ 200 kgf/m^2).

For the roads and sidewalks surrounding the construction site, considering the static load of subgrade grading, reinforced concrete, and asphalt concrete, as well as the live load from vehicular traffic and incorporating load safety factors, the approximate load of the nearby roads was estimated to be about 1 tf/m^2 (9.81 kN/m^3).

(5) Parameters for Diaphragm Wall, Buttress Wall, Cross Wall, Floor Slabs, and Foundation Slab

The earth-retaining structure in this study was represented by a diaphragm wall with a thickness of 1.2 m. Its penetration depth was 54 m on the south side and 52 m on the other three sides. Within the excavation zone, three Cross walls oriented from south to north, each with a thickness of 60 cm, were established. Additionally, there were eight buttress walls on both the north and south sides, each with a length of 10 m and a thickness of 60 cm. Four buttress walls, 12 m in length and 60 cm thick, were situated on both the east and west sides. The thickness of the floor slabs was 0.45 m, while the foundation slab was 1.2 m thick. The vertical distribution was designated as 1FL at −0.3 m, B1FL at −3.4 m, B2FL at −7.4 m, B3FL at −12.8 m, B4FL at −16.2 m, B5FL at −19.4 m, B6FL at −22.6 m, and FS at −25.7 m. The detailed configurations can be seen in Figure 11a,b and Figure 12b.

The modulus of elasticity for the diaphragm wall, buttress wall, Cross wall, floor slabs, and foundation slab employs the concrete's elasticity modulus $E_c = 150,000 \times \sqrt{f'_c} \times 9.8\ (\mathrm{kN}/cm^2)$. Here, f'_c signifies the 28-day compressive strength of the concrete. For the diaphragm wall, buttress wall, and Cross wall, f'_c is taken as 280 (kgf/cm^2), while for the floor and foundation slabs, it is taken as 350 (kgf/cm^2). When considering the stiffness of the aforementioned structures, it is noted that when these structures undergo substantial bending moments, their stiffness may vary due to concrete cracking. According to research by Ou [31], the wall stiffness should be multiplied by a reduction coefficient ranging from 0.6 to 0.8 for design purposes. Additionally, according to Ou [32] in "Advanced Deep Excavation Engineering Analysis and Design", it was suggested that under the same conditions, the influence of construction factors on floor slabs was relatively minor compared to the support, resulting in a smaller reduction in axial stiffness for the floor slabs

than for the support. Therefore, in this study, integrating the content of the aforementioned literature, a reduction coefficient of 0.6 was used for the diaphragm wall, buttress wall, and Cross wall, whereas a coefficient of 0.7 was adopted for the floor and foundation slabs. The selected parameters for these structures are presented in Table 9. In the PLAXIS 3D analysis, plate elements were employed to simulate the diaphragm wall, buttress wall, and Cross wall. It was assumed that these walls are homogeneous and perfectly bonded, without considering the possibility of construction defects.

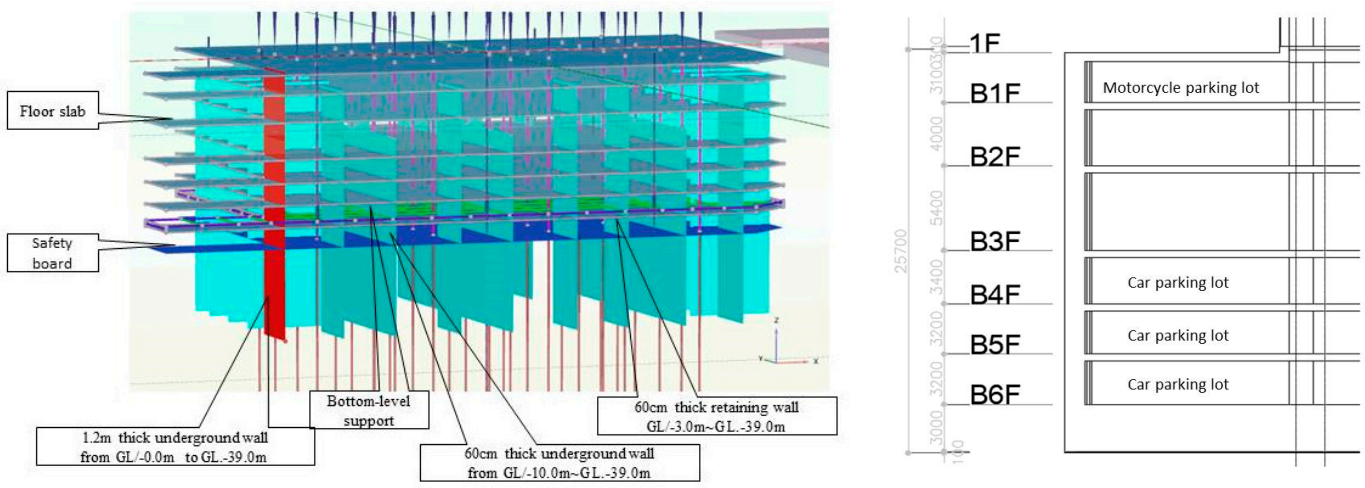

(**a**) (**b**)

Figure 11. (**a**) PLAXIS 3D configuration of Cross wall, buttress wall, and pile wall; (**b**) Elevation layout of floor and foundation slabs.

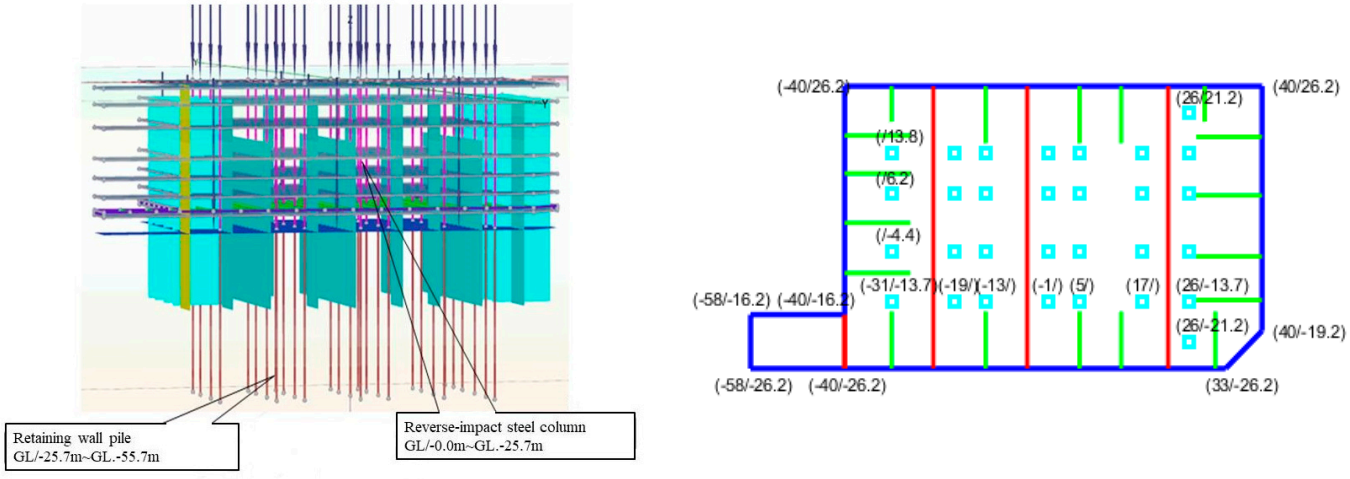

(**a**) (**b**)

Figure 12. (**a**) PLAXIS 3D configuration of Pile Wall and Top-Down Steel Columns; (**b**) Plan layout showing positions of the Pile Wall and Top-Down Steel Columns. (where, the blue line represents diaphragm wall, the green line represents buttress wall, and the red line represents cross wall).

(6) Pile Wall Parameter Configuration

In this project, the foundation employed pile walls with a thickness of 1.2 m. Their lengths range from 2.5 m to 5.0 m, with a depth of 30 m (from GL.−25.7 to GL.−55.7). To streamline the analysis, the foundation piles in this study were designed with dimensions of 1.2 m × 3.5 m × 30 m. For the PLAXIS 3D analysis, embedded beam elements were utilized to simulate the pile walls. The material parameters for these are provided in Supplementary Table S2.

Table 9. Parameters for the Diaphragm Wall, Buttress Wall, and Cross Wall.

Item	Thickness (m)	Unit Weight γ (kN/m^3)	Young's Modulus E (kN/m^2)	Poisson's ratio υ	f_c' (kg/cm^2)	Remark (Ou [32])
Diaphragm wall (DW)	1.2	24	1.48×10^7	0.17	280	Reduction coefficient of 0.6
Buttress walls, Cross walls (BW&CW)	0.6	24	1.48×10^7	0.17	280	Reduction coefficient of 0.6
Floors 1F to B6F Slabs	0.45	24	1.93×10^7	0.17	350	Reduction coefficient of 0.7
Foundation Slab (FS)	1.2	24	1.93×10^7	0.17	350	Reduction coefficient of 0.7

(7) Top-Down Construction Steel Column Parameter Configuration

The construction process employed in this project is the top-down method, which included 30 inverted steel support columns. Each column had dimensions of 1.2 m × 1.2 m, and their designed length was 28.7 m (from GL.0 to GL.−25.7, with an additional 3 m embedded into the pile wall). The columns were filled with self-compacting concrete with a compressive strength f_c' = 560 kg/cm^2. In the PLAXIS 3D analysis, beam elements were used to represent the top-down steel columns. The material parameters for these columns are detailed in Supplementary Table S3. The positioning of these columns can be seen in Figure 12.

(8) Bracing Parameter Configuration

According to the structural design data, horizontal steel bracing was erected at GL.−21.8 m. This bracing adopted a 2H414 × 405 × 18 × 28 steel profile with intervals less than or equal to 6 m. The surrounding structure utilized the same 2H414 × 405 × 18 × 28 steel profile, while diagonal bracing employed the H350 × 350 × 12 × 19 steel profile. Each bracing unit was pre-stressed with a load of 100 t. Based on the study by Ou [31], the stiffness of the bracing is appropriately reduced, with general reduction coefficients ranging between 0.5 to 0.7. In this research, the reduction coefficient for bracing stiffness was set at 0.7.

For the PLAXIS 3D analysis, top-down steel columns utilize beam elements, and the encirclement and bracing were simulated using node-to-node anchor elements. When simulating with beam elements, it was assumed that the steel profiles were homogenous, thus a linear condition was selected. The material parameters related to this are detailed in Supplementary Table S4. The positioning of these elements is illustrated in Supplementary Figure S2 and Figure 13.

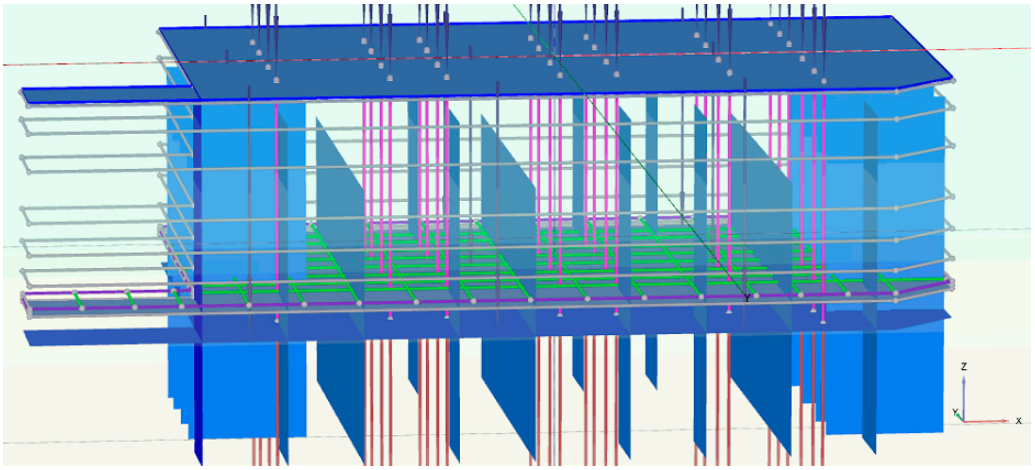

Figure 13. PLAXIS 3D Ground Level Horizontal Bracing Configuration.

3.3. Construction Steps

The construction procedure was simulated using Plaxis 3D 2018, broken down into ten distinct construction phases as illustrated in Figure 14. The purpose was to study the impact of excavation on lateral displacement changes, subsequently pinpointing the most accurate analytical method that aligns the simulation with real-world scenarios.

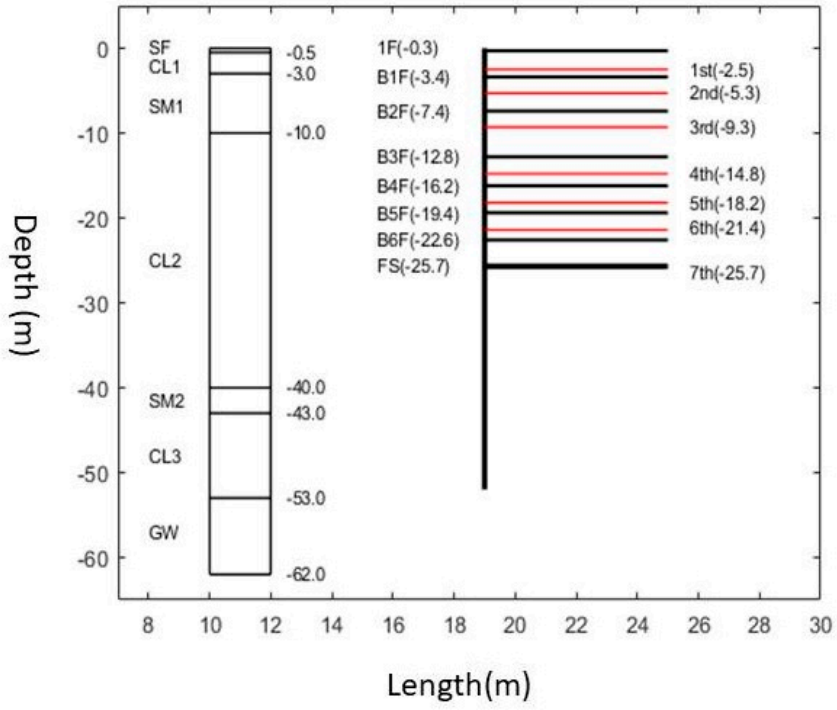

Figure 14. Excavation Construction Cross-Section.

The simulated construction phases encompass the following ten steps:

(1) Initial phase: Establishment of initial ground stresses.
(2) Phase 1:
    a. Load application from adjacent buildings and roads.
    b. Construction of diaphragm walls, cross walls, buttress walls, wall piles, and top-down steel columns, followed by zeroing displacements.
(3) Phase 2:
    a. First excavation to GL.−2.5 m, concurrently demolishing the metro exit cross wall to GL.−2.5 m.
    b. Dewatering corresponding with the excavation depth.
    c. Construction of 1F floor slab at GL.−0.3 m.
(4) Phase 3:
    a. Second excavation to GL.−5.3 m, with simultaneous removal of the buttress walls and metro exit cross wall to that depth.
    b. Corresponding dewatering.
    c. B1F floor slab establishment at GL.−3.4 m.
(5) Phase 4:
    a. Third excavation to GL.−9.3 m, with parallel demolition of the buttress walls and metro exit cross wall.
    b. Dewatering as per excavation.
    c. B2F floor construction at GL.−7.4 m.
(6) Phase 5:
    a. Fourth excavation to GL.−14.8 m, with concurrent demolition activities.

b. Relevant dewatering.
c. B3F floor establishment at GL.−12.8 m.

(7) Phase 6:

a. Fifth excavation to GL.−18.2 m, with simultaneous demolition tasks.
b. Dewatering in line with excavation.
c. B4F floor construction at GL.−16.2 m.

(8) Phase 7:

a. Sixth excavation to GL.−21.4 m, alongside demolition activities.
b. Associated dewatering.
c. B5F floor establishment at GL.−19.4 m.

(9) Phase 8:

a. Seventh excavation to GL.−22.6 m, in parallel with demolition.
b. Corresponding dewatering.
c. Horizontal bracing installation at GL.−21.8 m.

(10) Phase 9:

a. Eighth excavation reaching GL.−25.7 m, alongside the usual demolition tasks.
b. Dewatering to match excavation.
c. Foundation slab (FS) construction at GL.−25.7 m and B6 floor slab at GL.−22.6 m.
d. Removal of the horizontal bracing at GL.−21.8 m.

3.4. Analysis Results and Model Validation

This section elucidated the analysis results from the deep excavation simulation using the finite element software PLAXIS 3D2018 and their comparison with actual on-site measurements to verify the accuracy of the simulation.

1. Lateral Displacement Analysis and Comparison:

The excavation site had eight inclinometers within the wall, each measuring the wall displacement at various excavation stages. The study made a comparison for each. From the analysis, the trend in the deformation of the diaphragm wall was consistent. By the last stage (eighth stage) of excavation, the location and magnitude of maximum displacement in the simulation were approximately in line with the measurements. The detailed numerical comparisons are shown in Table 10.

Table 10. Comparison of Analysis Results with On-Site Maximum Displacement Measurements.

Inclinometer ID	HS Model (Plaxis 3D 2018)		Actual Monitoring Data		Remark
	Depth (Location)	Displacement Value	Depth (Location)	Displacement Value	
SID-1	−21.35 M	−5.06 mm	−22.00 M	−5.33 mm	North side
SID-2	−21.42 M	−5.68 mm	−23.00 M	−8.18 mm	North side
SID-3	−21.80 M	−7.06 mm	−18.00 M	−6.74 mm	East side
SID-4	−20.90 M	−3.51 mm	−21.00 M	−3.6 mm	East side
SID-5	−21.46 M	−5.52 mm	−25.00 M	−5.86 mm	South side
SID-6	−24.27 M	−7.76 mm	−25.00 M	−10.32 mm	South side
SID-7	−21.24 M	−3.23 mm	−21.00 M	−4.30 mm	South side
SID-8	−21.46 M	−6.73 mm	−25.00 M	−6.79 mm	West side

Displacement Negative Values on the Excavation Side. Location Negative Values Below Ground Level.

2. Settlement Analysis and Comparison:

Based on the road location, the excavation site was examined at three locations on the north side and two on the west, totaling five positions. The author has organized the

numerical analysis and actual monitoring values in Table 11. Observations from the table indicate that, regardless of whether it is on the north or west side, the maximum subsidence occurs in the eighth phase of excavation. Moreover, the results are all less than the 20 mm neighboring building settlement allowance specified by Taiwanese regulations [33].

Table 11. Stage-wise Excavation Settlement (PLAXIS Analyzed Values and Measured Values).

Point	Source	Phase 1 Excavation	Phase 2 Excavation	Phase 3 Excavation	Phase 4 Excavation	Phase 5 Excavation	Phase 6 Excavation	Phase 7 Excavation	Phase 8 Excavation
SM21~SM23	Analyzed Values	−13.52	−13.54	−13.42	−13.05	−13.13	−13.37	−13.91	−14.69
(North)	Measured Values	−8.8	−8.8	−12.6	−13.00	−13.00	−13.50	−13.90	−19.00
SM29~SM31	Analyzed Values	−13.76	−13.88	−13.90	−13.58	−13.65	−13.88	−14.49	−15.33
(North)	Measured Values	−8.0	−8.50	−9.90	−10.90	−11.30	−12.60	−13.60	−18.50
SM37~SM39	Analyzed Values	−13.11	−13.18	−13.14	−12.84	−12.92	−13.16	−13.72	−14.53
(North)	Measured Values	−8.7	−9.50	−10.80	−12.60	−12.00	−13.50	−14.30	−18.10
SM11~SM13	Analyzed Values	−12.16	−12.27	−12.43	−12.5	−12.66	−12.87	−13.27	−13.74
(West)	Measured Values	−5.10	−6.40	−7.50	−8.10	−9.20	−9.80	−11.10	−15.10
SM3~SM5	Analyzed Values	−13.17	−13.10	−12.97	−12.76	−12.89	−13.15	−13.58	−14.21
(West)	Measured Values	−7.30	−9.20	−10.90	−12.40	−13.30	−13.60	−14.60	−15.90

By comparing the results, it is evident that the site is rectangular in shape. The numerical simulation results for the shorter east-west sides of the site were closer to the actual measurements. For the longer north side, due to the even distribution of the strut and the diaphragm wall, the simulation results were also closely aligned with the measurements. However, for the south side, the uneven placement of the strut and the diaphragm wall, combined with the multiple corners, resulted in a more significant disparity between the simulation and the measurements. As per the research by Ou [19], the mechanism by which the strut suppresses wall displacement primarily arises from the friction between the strut and the soil, as well as the bearing capacity of the strut's end. This leads to a more complex mechanical behavior in the suppression of wall displacement by the strut, making simulations more challenging with reduced accuracy. Furthermore, because the counter-driven construction has a better capability of suppressing wall displacement, with deformations mostly below 10 mm, the measurements often deviate due to human error, making comparisons with simulation analyses less precise. Thus, trends in displacement are typically recognized. Comparisons of the numerical results for wall displacement and the trend in measurements are illustrated in Supplementary Figures S8–S15. Similarly, comparisons for settlement are shown in Supplementary Figures S3–S7.

4. Simulation Analysis of Timing for Removing Buttress Walls

Urban areas are densely populated with limited space. With the advent of subway systems and the burgeoning economic activities, many business activities have gradually moved underground, such as shopping streets and banquet halls. As a result, the height of a single underground floor has shifted from the traditional 3.2~3.4 m (typical of parking lots) to a more substantial 5~6 m to meet commercial demands. Therefore, controlling the deformation of the diaphragm wall has become increasingly crucial.

The primary function of the struts is to restrain the deformation of the diaphragm wall. While they are typically removed in stages based on excavation depth, this study proposed delaying the removal of the struts on the southern side of the B3F (with a height of 5.4 M)

until after the completion of B5FL, to simulate and analyze deformation differences (see Figure 14).

4.1. Simulation Steps

The simulation includes the following ten construction phases, as illustrated in Supplementary Materials (Figures S16–S19):

(1) Initial Phase: Establishment of the initial geotechnical conditions.

(2) Phase 1:
- Establishment of loadings from adjacent buildings and roads.
- Construction of Diaphragm Wall, cross walls, buttress walls, wall piles, and top-down steel columns, followed by resetting displacements to zero.

(3) Phase 2:
- First excavation to GL.−2.5 m while simultaneously demolishing the subway exit cross walls down to GL.−2.5 m.
- Dewatering in coordination with the excavation to GL.−2.5 m.
- Construction of the 1F floor slab at GL.−0.3 m.

(4) Phase 3:
- Second excavation to GL.−5.3 m, accompanied by the demolition of the buttress walls and subway exit cross walls down to GL.−5.3 m.
- Dewatering in sync with the excavation to GL.−5.3 m.
- Construction of the B1F floor slab at GL.−3.4 m.

(5) Phase 4:
- Third excavation to GL.−9.3 m, concurrently demolishing the buttress walls and subway exit buttress walls down to GL.−9.3 m.
- Dewatering in tandem with the excavation to GL.−9.3 m.
- Construction of the B2F floor slab at GL.−7.4 m.

(6) Phase 5:
- Fourth excavation to GL.−14.8 m, while simultaneously removing the buttress walls, cross walls, and subway exit buttress walls down to GL.−14.8 m, with a gradual demolition of the southern buttress walls.
- Dewatering in alignment with the excavation to GL.−14.8 m.
- Construction of the B3F floor slab at GL.−12.8 m.

(7) Phase 6:
- Fifth excavation to GL.−18.2 m, coinciding with the demolition of the buttress walls, cross walls, and subway exit buttress walls down to GL.−18.2 m.
- Dewatering alongside the excavation to GL.−18.2 m.
- Construction of the B4F floor slab at GL.−16.2 m.

(8) Phase 7:
- Sixth excavation to GL.−21.4 m, in conjunction with the removal of the retaining walls, cross walls, and subway exit buttress walls down to GL.−21.4 m.
- Dewatering congruent with the excavation to GL.−21.4 m.
- Construction of the B5F floor slab at GL.−19.4 m.

(9) Phase 8:
- Seventh excavation to GL.−22.6 m, simultaneous to the demolition of the retaining walls, cross walls, and subway exit buttress walls down to GL.−22.6 m.
- Dewatering in parallel with the excavation to GL.−22.6 m.
- Installation of horizontal bracing at GL.−21.8 m.

(10) Phase 9:

- Eighth excavation to GL.−25.7 m, accompanied by the removal of the retaining walls, cross walls, and subway exit buttress walls down to GL.−25.7 m, plus the demolition of the previously gradually removed southern buttress walls at B3F.
- Dewatering coordinated with the excavation to GL.−25.7 m.
- Construction of the foundation slab (FS) at GL.−25.7 m; Construction of the B6 floor slab at GL.−22.6 m.
- Dismantling of the horizontal bracing at GL.−21.8 m.

4.2. Analysis Results

The Displacement Reduction Ratio (DRR) was adopted as the metric for evaluating wall deformation. This ratio assesses the impact of different configurations on the lateral displacement of the diaphragm wall, as expressed in Equation (6):

$$\mathrm{DRR} = \frac{\delta_{hm,0} - \delta_{hm}}{\delta_{hm,0}} \times 100\% \quad (6)$$

where: $\delta_{hm,0}$: represents the maximum lateral displacement when the strut is removed with the excavation, δ_{hm}: is the maximum lateral displacement when the strut's removal is delayed based on functional requirements.

1. On the direct southern side, analysis from HS-5 (Figure A1) indicates:
   - Maximum lateral displacement with immediate strut removal was 5.52 mm.
   - Delaying B3F strut removal until after B5F completion resulted in a maximum lateral displacement of 5.30 mm.
   - This leads to a difference of 0.22 mm and a DRR of 3.98%. One reason might be the proximity to the margin and the reinforcing effect of the vertical diaphragm wall.
2. For the southeast side, as deduced from HS-6 (Figure A2):
   - Maximum lateral displacement with immediate strut removal was 7.76 mm.
   - With the delayed removal approach, it reduced to 3.63 mm.
   - The displacement difference amounted to 4.13 mm, with a DRR of 53.22%. This could be due to its central location on the diaphragm wall.
3. On the southwest side, data from HS-7 (Figure A3) reveals:
   - The maximum lateral displacement with immediate strut removal was 3.23 mm.
   - The delayed approach yielded a displacement of 3.15 mm.
   - This equates to a 0.08 mm difference and a DRR of 2.47%. This might be attributed to its proximity to the edge, leading to reduced deformation due to the reinforcing effect of the vertical diaphragm wall.

5. Conclusions

5.1. Conclusions

1. Conclusions derived from numerical analysis simulation and validation include:
   - The site in question is rectangular in shape. Simulation results on the shorter east-west sides closely match observed data. On the northern longer side, due to evenly spaced retaining and diaphragm walls, the simulated results also align closely with observations. However, for the southern longer side, which features irregularly placed retaining and diaphragm walls with multiple corner transitions, there is a notable difference between the simulation and observed data.
   - According to the research by Ou [19], the mechanism by which retaining walls control wall displacement primarily stems from the friction between the retaining wall and the soil, as well as the bearing capacity at the end of the retaining wall. This leads to a complex mechanical behavior, making simulations more challenging and less accurate.

- Additionally, top-down construction methods tend to offer better control over wall displacement. However, monitoring often entails human errors, resulting in imprecisions between simulations and observed values. As a result, trends rather than actual measurements in displacement are often relied upon for verification.
- The study indicates that the trend in lateral displacement is consistent with numerical analysis results. For surface subsidence, the observed values exceeded simulation predictions due to repeated resurfacing of the adjacent AC road. When factoring in the effects of repeated road resurfacing and observational errors, the analytical results can be considered consistent with the actual situation.

2. Conclusions regarding the timing of retaining wall removal include:
   - On the direct southern side, analysis from HS-6 shows a Displacement Reduction Rate (DRR) of 53.22%. This can be attributed to its position between the Diaphragm Wall, which inherently exhibits larger displacements and thus has more pronounced reduction effects.
   - On the southeast side, HS-5 analysis indicates a DRR of 3.98%. Being closer to the edge, and influenced by the reinforcing effects of the vertical Diaphragm Wall, the inherent displacements are smaller, leading to less significant reduction effects.
   - On the southwest side, analysis from HS-7 reveals a DRR of 2.47%. Similar to the southeast side, being closer to the edge and under the influence of the vertical Diaphragm Wall, the inherent displacements are minimal, resulting in less pronounced reduction effects.

5.2. Recommendations

1. Simulations indicate that adjusting the removal timing of retaining walls based on functional needs and linking them to floor slabs to form a T-shaped structure can effectively control wall displacement. For deeper basement levels, where temporary support is not available, this method can be considered to minimize displacement.
2. This study solely analyzed the staggered removal of the B3F southern retaining wall. Future studies could consider not removing all retaining walls and analyzing the relationship with wall thickness. If the results are significant, adjustments to the retaining wall's thickness could be made, potentially reducing construction costs or incorporating it as a permanent structural component.
3. Typically, in top-down projects during the final excavation phase, due to a longer unsupported length from deeper excavations, horizontal or diagonal bracing is required to control lateral wall displacement. However, this procedure is time-consuming and poses higher operational risks, increasing construction hazards. Future studies might explore the effects of not removing retaining and diaphragm walls during the final excavation phase on wall displacement control.

Supplementary Materials: The following supporting information can be downloaded at: https://www.mdpi.com/article/10.3390/buildings13112678/s1, Figure S1: Borehole Plan Layout and Cross-Section Line; Figure S2: Ground Level Horizontal Bracing Layout; Figure S3: Comparison of Ground Subsidence Analysis and Monitoring Results for Each Excavation Phase on the Northeast Side; Figure S4: Comparison of Ground Subsidence Analysis and Monitoring Results for Each Excavation Phase on the North Side; Figure S5: Comparison of Ground Subsidence Analysis and Monitoring Results for Each Excavation Phase on the Northwest Side; Figure S6: Comparison of Ground Subsidence Analysis and Monitoring Results for Each Excavation Phase on the Southwest Side; Figure S7: Comparison of Ground Subsidence Analysis and Monitoring Results for Each Excavation Phase on the Northwest Side; Figure S8: Comparison of Numerical Analysis Results with Monitoring Values from Monitoring Point SID 1; Figure S9: C omparison of Numerical Analysis Results with Monitoring Values from Monitoring Point SID 2; Figure S10: Comparison of Numerical Analysis Results with Monitoring Values from Monitoring Point SID 3; Figure S11: Comparison of Numerical Analysis Results with Monitoring Values from Monitoring Point SID 4; Figure S12: Comparison of Numerical Analysis Results with Monitoring Values from Monitoring Point SID-5;

Figure S13: Comparison of Numerical Analysis Results with Monitoring Va lues from Monitoring Point SID 6; Figure S14: C omparison of Numerical Analysis Results with Monitoring Values from Monitoring Point SID 7; Figure S15: C omparison of Numerical Analysis Results with Monitoring Values from Monitoring Point SID 8; Figure S16: Schematic Diagram of the Timing Steps for Removing Buttress Walls (Step 1 to Step 2); Figure S17: Schematic Diagram of the Timing Steps for Removing Buttress Walls (Step 3 to Step 4); Figure S18. Schematic Diagram of the Timing Steps for Removing Buttress Walls (Step 5 to Step 6); Figure S19 Schematic Diagram of the Timing Steps for Removing Buttress Walls (Step 7 to Step 9); Figure S20: Plaxis 3D Simulation Diagram for Buttress Wall Removal Timing; Figure S21: Plaxis 3D Analysis Location Diagram; Table S1: Simplified Soil Layer Parameter Table; Table S2: Material parameters for the Pile Wall (Embedded Beam); Table S3: Material parameters for the Top-Down Steel Column (Beam); Table S4: Node-to-Node Anchor Material Parameters.

Author Contributions: Conceptualization, C.-F.H., C.-F.K. and S.-L.C.; Methodology, C.-F.K. and S.-L.C.; formal analysis, C.-F.K.; investigation, C.-F.K.; writing—original draft preparation, C.-F.K. and C.-F.H.; writing—review and editing, C.-F.H. All authors have read and agreed to the published version of the manuscript.

Funding: This research received no external funding.

Data Availability Statement: The data used in this article are public.

Conflicts of Interest: The authors declare no conflict of interest.

Appendix A

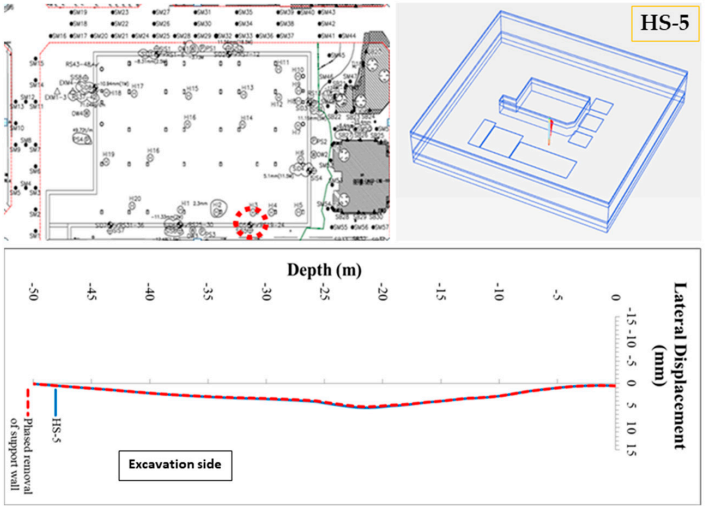

Maximum Displacement of the Diaphragm Wall		
Location	**Depth**	**Displacement**
HS-5	−21.46 M	5.52 mm
Gradual Removal of Retaining Wall	−21.46 M	5.30 mm
Difference		0.22 mm
B3F Diaphragm wall Displacement		
Location	**Depth**	**Displacement**
HS-5	−11.8 M	3.28 mm
Gradual Removal of Retaining Wall	−11.8 M	3.25 mm
Difference		0.03 mm
Note: Positive displacement values represent the excavation side. Negative depth values indicate below ground level.		

Figure A1. Comparison of Displacement between Gradual Removal and Simultaneous Removal of Buttress Walls on the Southeast Side.

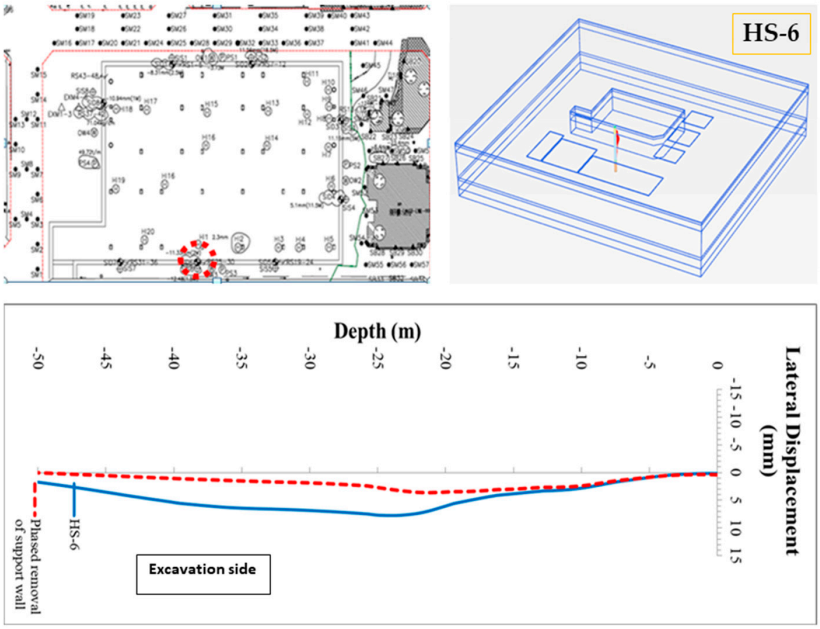

Maximum Displacement of the Diaphragm wall		
Location	**Location**	**Location**
HS-6	−24.27 M	7.76 mm
Gradual Removal of Retaining Wall	−21.43 M	3.63 mm
Difference		4.13 mm
B3F Diaphragm wall Displacement		
Location	**Location**	**Location**
HS-6	−11.8 M	3.19 mm
Gradual Removal of Retaining Wall	−11.8 M	2.64 mm
Difference		0.55 mm
Note: Positive displacement values represent the excavation side. Negative depth values indicate below ground level.		

Figure A2. Comparison of Displacement between Gradual Removal and Simultaneous Removal of Buttress Walls on the South Side.

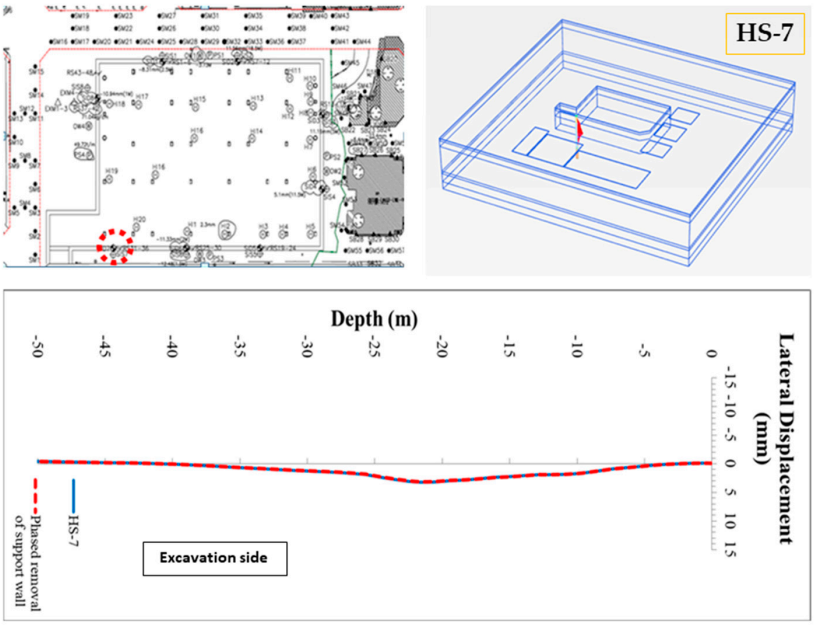

Figure A3. *Cont.*

Maximum Displacement of the Diaphragm wall		
Location	**Location**	**Location**
HS-7	−21.24 M	3.23 mm
Gradual Removal of Retaining Wall	−21.24 M	3.15 mm
Difference		0.08 mm
B3F Diaphragm wall Displacement		
Location	**Location**	**Location**
HS-7	−11.8 M	1.89 mm
Gradual Removal of Retaining Wall	−11.8 M	1.89 mm
Difference		0.00 mm
Note: Positive displacement values represent the excavation side. Negative depth values indicate below ground level.		

Figure A3. Comparison of Displacement between Gradual Removal and Simultaneous Removal of Buttress Walls on the Southwest Side.

References

1. Jian, Z.; Olivia, K. An introduction to connectivity concept and an example of physical connectivity evaluation for underground space. *Tunn. Undergr. Space Technol.* **2016**, *55*, 205–213. [CrossRef]
2. Hsieh, P.-G.; Ou, C.-Y.; Lin, Y.-K.; Lu, F.-C. Lessons learned in design of an excavation with the installation of buttress walls. *J. GeoEng.* **2015**, *10*, 63–73.
3. Shi, J.; Liu, G.; Huang, P.; Ng, C.W.W. Interaction between a large-scale triangular excavation and adjacent structures in Shanghai soft clay. *Tunn. Undergr. Space Technol.* **2015**, *50*, 282–295. [CrossRef]
4. Hong, Y.; Ng, C.W.W.; Liu, G.B.; Liu, T. Three-dimensional deformation behaviour of a multi-propped excavation at a "greenfield" site at Shanghai soft clay. *Tunn. Undergr. Space Technol.* **2015**, *45*, 249–259. [CrossRef]
5. Chen, R.; Meng, F.; Li, Z.; Ye, Y.; Ye, J. Investigation of response of metro tunnels due to adjacent large excavation and protective measures in soft soils. *Tunn. Undergr. Space Technol.* **2016**, *58*, 224–235. [CrossRef]
6. Whittle, A.; Davies, R. Nicoll Highway collapse: Evaluation of geotechnical factors affecting design of excavation support system. In Proceedings of the International Conference on Deep Excavations, Singapore, 28–30 June 2006; p. 30.
7. Abdi, A.S.; Ou, C.-Y. Numerical Study of the Effect of Ground Improvement on Basal Heave Stability for Deep Excavations in Normally Consolidated Clays. *J. Geotech. Geoenviron. Eng.* **2023**, *149*, 04023042. [CrossRef]
8. Mana, A.I.; Clough, G.W. Prediction of movements for braced cuts in clay. *J. Geotech. Eng. Div.* **1981**, *107*, 759–777. [CrossRef]
9. Ou, C.-Y.; Hsieh, P.-G.; Chiou, D.-C. Characteristics of ground surface settlement during excavation. *Can. Geotech. J.* **1993**, *30*, 758–767. [CrossRef]
10. Clough, G.W.; O'Rourke, T.D. *Construction-Induced Movements of In Situ Wall, Design and Performance of Earth Retaining Structure*; ASCE: Reston, VA, USA, 1990; pp. 439–470.
11. Masuda, T.; Einstein, H.H.; Mitachi, T. Prediction of lateral deflection of diaphragm wall in deep excavations. *Doboku Gakkai Ronbunshu* **1994**, *1994*, 19–29. [CrossRef] [PubMed]
12. Wu, P.-Z.; Wang, M.-J.; Peng, Y.-R. Investigation of Continuous Wall Deformation Behavior. In Proceedings of the 7th Geotechnical Engineering Research Symposium, Taiwan, 7–11 September 1997; pp. 601–608.
13. Wang, J.-Z.; Chan, X.-S.; Lei, Y.-M. Analysis of Soil Parameters in the Kaohsiung Metro Red Line Section. *J. Chin. Inst. Civ. Hydraul. Eng.* **2003**, *30*, 101–104.
14. Surarak, C. *Geotechnical Aspects of the Bangkok MRT Blue Line Project*; Griffith University: Nathan, Australia, 2011.
15. Peck, B. Deep excavation and tunnelling in soft ground, State of the art volume. In Proceedings of the 7th ICSMFE, Mexico City, Mexico, 29 August 1969; pp. 225–290.
16. Ou, C.-Y.; Chiou, D.-C.; Wu, T.-S. Three-dimensional finite element analysis of deep excavations. *J. Geotech. Eng.* **1996**, *122*, 337–345. [CrossRef]
17. Ou, C.; Liao, J.; Lin, H. Performance of a topdown basement construction. *J. Geotech. Geoenviron. Eng.* **1998**, *9*, 798–808. [CrossRef]
18. Avanti, A. *Numerical Analyses of Jakarta MRT Deep Excavation Project*; National Taiwan University of Science and Technology: Taipei, Taiwan, 2013.
19. Ou, C.-Y. Finite element analysis of deep excavation problems. *J. Geoengin.* **2016**, *11*, 1–12.
20. Liao, R.-T. *Performances of a Top Down Deep Excavation*; National Taiwan University of Science and Technology: Taipei, Taiwan, 1996.
21. Wang, J.-Z. *Undrained Creep Behavior of Soft Clay Induced by Deep Excavation*; National Taiwan University of Science and Technology: Taipei, Taiwan, 1997.
22. Hsieh, P.-G. *Prediction of Ground Movements Caused by Deep Excavation in Clay*; National Taiwan University of Science and Technology: Taipei, Taiwan, 1999.
23. Hsieh, P.-G.; Lin, Y.-L.; Ou, C.-Y. Three-Dimensional Numerical Analysis and Performance of Deep Excavation with Cross Walls and Buttress Walls. *J. Chin. Inst. Civ. Hydraul. Eng.* **2010**, *22*, 11–22. [CrossRef]

24. Chen, S.-L.; Ho, C.-T.; Li, C.-D.; Gui, M.-W. Efficiency of buttress walls in deep excavations. *J. GeoEng.* **2011**, *6*, 145–156.
25. Khoiri, M.; Ou, C.-Y. Evaluation of deformation parameter for deep excavation in sand through case histories. *Comput. Geotech.* **2013**, *47*, 57–67. [CrossRef]
26. Ou, C.-Y.; Hsieh, P.-G.; Lin, Y.-L. A parametric study of wall deflections in deep excavations with the installation of cross walls. *Comput. Geotech.* **2013**, *50*, 55–65. [CrossRef]
27. Ye, C.-Y. *Efficiency of Buttress Walls and Cross Walls in Deep Excavation*; National Taipei University of Technology: Taipei, Taiwan, 2012.
28. Fong, J.-W. *Numerical Analysis of Buttress Walls and Cross Walls in Deep Excavation*; National Taipei University of Technology: Taipei, Taiwan, 2015.
29. Hsieh, P.-G.; Ou, C.-Y. Shape of ground surface settlement profiles caused by excavation. *Can. Geotech. J.* **1998**, *35*, 1004–1017. [CrossRef]
30. Ladd, R.S. Specimen Preparation and Cyclic Stability of Sands. *J. Geotech. Eng. Div.* **1977**, *103*, 535–547. [CrossRef]
31. Ou, C.-Y. *Deep Excavation Engineering: Analysis, Design Theories and Practices*; Science and Technology Books: Taipei, Taiwan, 2002.
32. Ou, C.Y. *Advanced Deep Excavation Engineering Analysis and Design*; Tech Books Incorporated: Taipei, Taiwan, 2017.
33. Civil Engineering Association of Taipei City. *Practical Manual for Excavation and Earth Retaining Support Engineering Design*; Civil Engineering Association of Taipei City: Taipei, Taiwan, 2002.